

FDC: Fast KV Dimensionality Compression for Efficient LLM Inference

Zeyu Zhang
University of Virginia
USA

Haiying Shen
University of Virginia
USA

Abstract

In large-language models, memory constraints in the Key-Value Cache (KVC) pose a challenge during inference. In this work, we propose FDC, a fast KV dimensionality compression system that eliminates the decompression overhead incurred in the existing KV dimensionality compression system, Palu, and reduces attention time. Moreover, FDC employs adaptive compression, tailoring KV compression rates across heads and layers based on their contributions to inference to maximize overall compression while maintaining an accuracy loss constraint. Additionally, FDC enhances the attention kernel to balance the uneven workloads caused by the adaptive compression approach to further reduce attention computation latency. Comprehensive experiments demonstrate that compared to Palu, FDC can reduce Job Completion Time (JCT) by up to 64%, and delivers up to $1.97\times$ throughput under the same latency, while maintaining 99% of the accuracy without compression. When state-of-the-art eviction and quantization methods are combined with FDC, they exhibit similar improvements compared to those combined with Palu. We open-sourced the code.

Keywords: KV cache, compression, inference, acceleration

1 Introduction

Generative large language models (LLMs) [1–6] have transformed natural language processing (NLP), showcasing remarkable performance across various tasks like text completion [7], dialogue generation [8], code synthesis [9], language translation [10], text summarization [11–13], and document classification [14, 15]. The LLM models are primarily inspired by the transformer architecture [16], which employs attention to capture long-range dependencies in sequences.

During LLM inference, text generation starts with providing a prompt. LLM generates the first token via prompt processing (a.k.a., prefill), followed by text generation (a.k.a., decode) to generate new tokens. LLMs typically consist of multiple transformer layers, where each layer receives an embedding matrix E for the entire input. These embeddings are projected to produce Query (Q), Key (K), and Value (V) components for each token, serving as inputs to the attention layer. The KV values of newly generated tokens are stored in the Key-Value Cache (KVC) to avoid redundant computations. During token generation, the KV values of previous tokens are fetched from the KVC and fed into the attention layer. The resulting attention output guides token generation.

The primary challenge of LLM inference is memory constraints within KVC, which limits GPU utilization and consequently decreases throughput. To address it, various KV compression methods have been proposed and they can be divided into two main categories: token eviction methods [17–26], quantization methods [27–31], and low-rank approximation methods [32]. Token eviction methods remove the KV values of unimportant tokens that have minimal impact on the inference results. Quantization methods compress KV values by reducing the bit width of each element in the KV matrix from a higher bit width (e.g., float16) to a lower bit width (e.g., 4-bit, 2-bit). However, these methods overlook the redundancy inherent in KV representations [32]. By leveraging this redundancy, it is possible to represent KV using fewer hidden dimensions, thereby achieving compression without incurring significant information loss. Recently, Palu [32] employs low-rank approximation to compress the hidden dimensions of KV. This approach is complementary to eviction and quantization methods and can be integrated with them to enhance the KV compression rate further [32]. InfiniGen [24] uses low-rank approximation to analyze attention scores and identify unimportant tokens efficiently; however, it is fundamentally an eviction method.

Currently, state-of-the-art LLMs adopt Rotary Positional Embedding (RoPE) [33] to inject positional information into tokens’ Q and K . However, as explained in §2, the presence of RoPE necessitates that Palu first decompress the compressed K before RoPE, and only then can the RoPE-processed K be fed into the attention. This leads to two main issues: 1) an unavoidable K -decompression overhead, and 2) the inability to directly use the compressed K to accelerate attention [32]. Because many LLM tasks, such as summarization, book generation, and Information Retrieval (IR), involve long-sequence processing [34–36], the context window length of state-of-the-art LLMs now extends to 128K or even 1M tokens [37–41]. Long sequences amplify Palu’s K -decompression overhead and the attention overhead. Experimental results in §3.1 show that for input lengths up to 100K, Palu’s attention computation can account for up to 36.3% and 31.9% of the Job Completion Time (JCT) during the prefill and decode phases, respectively, and decompressing K during the decode phase can reach up to 19.7% of the JCT. For output lengths up to 100K, Palu’s attention computation in the decode phase can climb to 74.6% of the JCT, while the time to decompress K can reach up to 29.5%.

We propose FDC to tackle these issues. FDC is a Fast KV Dimensionality Compression system, which not only eliminates the K -decompression overhead but also reduces attention time for KV dimensionality compression. FDC comprises three key components as below.

Post-RoPE QK compression for decompression elimination and attention acceleration. Unlike Palu, which compresses QK before RoPE, FDC compresses QK after RoPE. In §3.2, we observe that the post-RoPE QK is also compressible, which is determined by the model itself rather than the input tokens. As a result, a rotation matrix R suitable for compressing post-RoPE QK can be precomputed offline. During online inference, the post-RoPE QK is compressed using R , and the compressed QK is fed directly into attention, eliminating the decompression of K . Attention is computed on the compressed QK, reducing its computation time.

Adaptive compression rate. Model layers contribute differently to the output [16], as do the attention heads within each layer [18]. Thus, FDC applies different compression rates to QKV in different heads and layers to maximize the overall KV compression rate given an accuracy constraint. These compression rates are determined by the magnitude of the components in each dimension of the compressed QKV vectors.

Attention kernel enhancement for adaptive compression rate. The different compression rates on the hidden dimensions of QKV in FDC can lead to imbalanced execution times across a GPU’s Stream-Multiprocessors (SM). Thus, FDC balances the uneven workloads across SMs for attention in the prefill and decode phases, respectively, to further reduce attention computation latency.

In summary, our work has the following contributions:

- We conduct extensive experiments with numerous state-of-the-art models and complex-task datasets to demonstrate the rationality and feasibility of FDC’s design principles and provide geometric explanations for these observations.
- We propose FDC, a fast KV dimensionality compression system that eliminates the K -decompression overhead and accelerates attention. It can complement existing token eviction based and quantization based KV compression methods.
- Comprehensive experiments demonstrate that compared to Palu, FDC can reduce JCT by up to 64%, Time-To-First-Token (TTFT) by up to 35%, and Time-Between-Token (TBT) by up to 64%, and delivers up to 1.97× throughput under the same latency, while maintaining 99% of the accuracy without compression. When the state-of-the-art eviction and quantization methods are combined with FDC, they exhibit similar improvements compared to those combined with Palu.

We open-sourced the code of FDC [42].

2 Background

We explain how the current work compresses KV along the hidden dimension. Table 1 lists notations used in the paper.

d	Model dimension size	N_h	The number of heads
N_l	The number of layers	d_h	Head dimension size ($= d/N_h$)
E	Token embeddings	Q	Query matrix
K	Key matrix	V	Value matrix
R	Rotation matrix	p	Compression rate
W	Parameter matrix	s	Sequence length

Table 1. Notations used in the paper.

The common way to compress the hidden dimension of KV is first applying Singular Value Decomposition (SVD) [43] to the parameter matrices that generate KV [32]. Because the procedures for K and V are identical, we describe the process for K only. Let $K = EW$, where W is the parameter matrix for K . The shapes of E and W are $s \times d$ and $d \times d_h$, respectively. Decomposing W via SVD yields two matrices A and B such that $W = AB$, with shapes $d \times k$ and $k \times d_h$, where $k < d_h$. The original K has shape $s \times d_h$. During compression, the compressed K' is generated via $K' = EA$, whose shape is $s \times k$. Because $k < d_h$, K' is smaller than K , achieving the desired compression. To reconstruct an approximation of the original K , K' and B are multiplied, i.e., $K'B \approx K$. Palu [32] is the state-of-the-art and representative method that employs this form of KV compression.

Currently, the state-of-the-art transformer-based LLMs employ RoPE [33] to encode positional information for tokens. RoPE processes the generated Q and K . Specifically, RoPE rotates each row vector \mathbf{q} and \mathbf{k} of Q and K using a rotation matrix H_i , where i is the position of \mathbf{q} and \mathbf{k} in the sequence. Without RoPE, the computation QK^T in attention can be rewritten as $EW_Q(EW_K)^T = EW_Q(EA_K B_K)^T = E(W_Q B_K^T)K'^T$, where W_Q and B_K are merged together offline to remove the online decompression overhead for multiplying B_K [32]. And K' can be used directly in attention to reduce the computation time. However, the existence of RoPE prevents the integration of B_K into W_Q because QK^T in attention is changed to $\text{RoPE}(Q)\text{RoPE}(K)^T$ [32]. Therefore, Palu keeps the decompression process $K'B_K$ before RoPE, which introduces the decompression overhead for K' . Besides this, Palu’s attention takes $\text{RoPE}(Q)$ and $\text{RoPE}(K)$ as inputs for computation. Hence, the attention cannot leverage the compressed K' for acceleration. Long sequences can amplify this decompression overhead and attention time. We explain it in §3.

3 Motivation

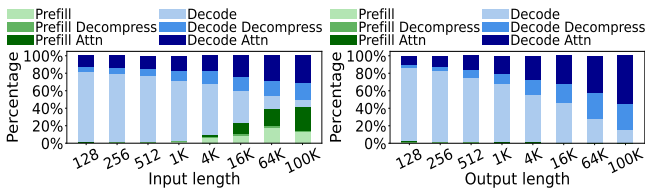
In this section, we analyze Palu’s K -decompression overhead as well as the overhead associated with attention computation for RoPE-based models, and we highlight potential opportunities for optimizing Palu.

3.1 Decompression and Attention Overhead of Palu

We first selected the largest model with 128K context window length, Llama-3.1 70B, from Table 5 to examine the percentage of each JCT component under different input and output lengths. The ranges for input and output lengths were determined based on the dataset information in Table 6. When varying input and output lengths, the corresponding output length and input length were set to 256, which are the common lengths in datasets in Table 6. Fig. 1 illustrates the JCT decomposition of Palu under various input and output length settings for Llama-3.1 70B.

Fig 1(a) shows that as the input length increases from 128 to 100K, the time spent in decompressing K during the decode phase grows from 5.6% to 19.7% of the JCT. The percentage of attention time during the prefill phase rises from 0.4% to 26.3% of the JCT, and the percentage of attention time during the decode phase increases from 13.1% to 29.5%. This is because, with longer input lengths, the overhead of decompressing K in the decode phase grows, and the attention computation overhead during both prefill and decode phases also increases. The decompression time during the prefill phase accounts for no more than 2% of the JCT, mainly because the prefill phase has only one iteration (and thus decompresses K only once), unlike the decode phase that involves multiple iterations.

Fig. 1(b) shows that as the output length increases from 128 to 100K, the proportion of attention computation during decode grows from 11.3% to 55.7% of the JCT, while the time spent in decompressing K increases from 4.4% to 29.5% of the JCT. This occurs because a longer output length leads to larger K , increasing both the attention computation time and the time required to decompress K . The prefill time remains under 2% of the JCT, which is due to the large number of decode iterations (associated with a long output), causing the prefill phase to account for only a small fraction of JCT. Therefore, in the case of long output lengths, the main focus should be on improving the decode phase.



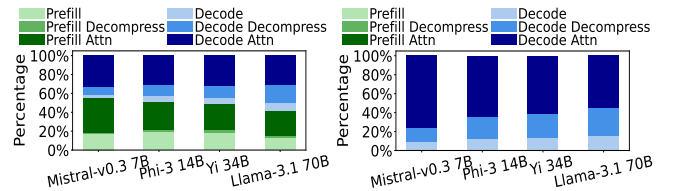
(a) Output length 256 with varying (b) Input length 256 with varying out-
input lengths. put lengths.

Figure 1. Palu’s JCT decomposition for Llama-3.1 70B with different input and output lengths.

Additionally, we employed various models to investigate how a long input length and a long output length influence the components of JCT. The models used are those in Table 5 that support a context window length of 128K. Fig. 2(a) illustrates the scenario where the input length is 100K and the output length is 256. As the model size increases from

7B to 70B, the attention computation time during the prefill and decode phases drops from 36.3% and 31.9% of JCT, respectively, to 26.3% and 29.5%. This is because a larger model has a larger hidden dimension d , which causes the linear operations that scale quadratically with d to occupy a greater portion of the total time (whereas attention scales linearly with d). Meanwhile, the time spent in decompressing K during decode increases from 10.5% to 19.7% of the JCT, as a larger d leads to a larger-sized K and thus more decompression time. During the prefill phase, the decompression time remains under 2.2% of the JCT, for the same reason described when discussing Fig. 1(a).

Fig. 2(b) illustrates the case where the input length is 256 and the output length is 100K. As the model size increases from 7B to 70B, the attention time during decode decreases from 74.6% to 55.7% of the JCT, while the decompression time increases from 14.4% to 29.5%. This is the same reason as given for Fig. 2(a).



(a) Input length 100K and output (b) Input length 256 and output
length 256. length 100K.

Figure 2. Palu’s JCT decomposition for different models.

Overall, long sequences amplify both Palu’s attention overhead and the overhead associated with decompressing K . For input lengths up to 100K, Palu’s attention computation can account for up to 36.3% and 31.9% of the JCT during the prefill and decode phases, respectively, and decompressing K during the decode phase can reach up to 19.7% of the JCT. For output lengths up to 100K, Palu’s attention computation in the decode phase can climb to 74.6% of the JCT, while the time to decompress K can reach up to 29.5%.

3.2 Opportunities

To reduce the attention overhead, it is desirable to perform computation directly using the compressed K . Doing so also avoids the computational cost of decompressing K prior to the attention. Therefore, we may consider compressing K after it has been processed by RoPE. However, this approach should not introduce additional overhead at the end of the attention computation; otherwise, the benefits gained from removing K decompression would be diminished.

Let us denote the post-RoPE Q and K as Q_p and K_p , respectively. Suppose there is a rotation matrix R with shape $d_h \times d_h$. Then, the attention computation $Q_p K_p^T$ is mathematically equivalent to $(Q_p R)(K_p R)^T$ since $(Q_p R)(K_p R)^T = Q_p (R R^T) K_p^T = Q_p K_p^T$. In other words, computing $Q_p K_p^T$ can be reformulated as multiplying $Q_p R$ and $K_p R$. If the matrix

R rotates all row vectors of Q_p and K_p such that the resulting vectors contain many low-magnitude dimensions, those dimensions can be removed to compress Q_p and K_p without much information loss. This allows us to compute an approximate value of $Q_p K_p^T$ directly by multiplying the compressed versions of Q_p and K_p . This approach will be detailed in §5.

However, achieving this objective requires satisfying two conditions. First, Q_p and K_p must be compressible. That is, there must exist a common rotation matrix R such that the rotated versions ($Q_p R$ and $K_p R$) contain many low-magnitude dimensions whose removal does not significantly distort the data. Second, the common R used for Q_p and K_p should be model-specific and independent of the tokens. In other words, given a model, this common R can be determined offline and will not vary with the dataset. These two conditions raise two critical questions.

- 1) Does there exist a common R that can compress Q_p and K_p without significantly distorting the data?
- 2) Is the common R that Q_p and K_p share model-specific and independent of the tokens?

The answer to both questions is yes. We will address them in the following observations, which give us opportunities for optimizing Palu.

Does there exist a common R that can compress Q_p and K_p without significantly distorting the data? We observe that the answer is yes. In the NLP domain, it is common to apply SVD directly to a matrix X composed of row vectors (e.g., word embeddings). This decomposition yields singular values and an R , which can then be used to compress X . This approach is detailed in §4.1. The magnitudes of the singular values reflect the magnitude of the row vectors of XR along each dimension. If many singular values approach zero, it indicates that XR contains a large number of low-magnitude dimensions that can be discarded without significantly distorting the data.

Following this approach, we combine the row vectors of Q_p and K_p into a single matrix and calculate its singular values and R for each attention head. Fig 3 shows the average singular values across all attention heads for different models in Table 5 and datasets in Table 6. We observe that the average singular values in the leftmost dimensions are significantly higher than those in other dimensions, indicating that the row vectors of $Q_p R$ and $K_p R$ have many small-magnitude dimensions whose removal does not change the vectors much. The explanation for this observation will be detailed in §4.2.

Is the common R that Q_p and K_p share model-specific and independent of the tokens? We observe that the answer is yes. To investigate this question, we need to examine whether the matrices R generated from different datasets are similar. If R is independent of the token, then the R derived from different datasets should exhibit a certain degree of similarity. Moreover, the R computed based on randomly

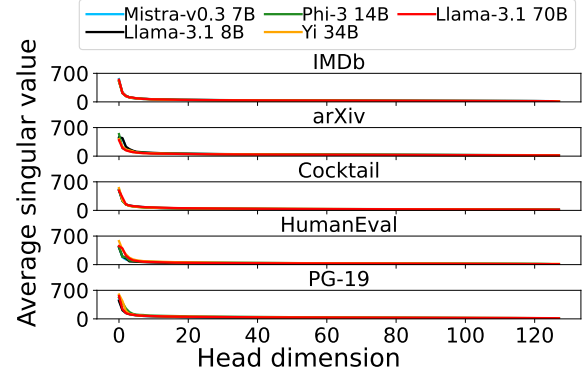


Figure 3. The average singular value for the Q_p - K_p pair.

generated tokens should also resemble these R derived from datasets. To validate this, we randomly generate a sequence of tokens from the vocabulary, with the total number of tokens matching that of a randomly selected dataset. Based on these random tokens, we compute a rotation matrix R_r . Each dataset yields its own R . We then measure the degree of difference between each dataset-specific R and R_r . This difference is quantified by the ratio of the deviation in each element of R to its magnitude, where smaller ratios indicate lower degrees of difference.

Specifically, given a model, each head h in layer l has an $R_r^{h,l}$ generated from random tokens and an $R_a^{h,l}$ from a dataset a . We use $\text{AABS}(M)$ to denote the average absolute value of all elements in matrix M and $\text{SUB}(M_1, M_2)$ to denote the element-wise subtraction of M_2 from M_1 . For a model and a dataset a , we compute $\bar{\epsilon} = \frac{1}{N_h N_l} \sum_{h=1}^{N_h} \sum_{l=1}^{N_l} \text{AABS}(R_a^{h,l})$ to evaluate the average magnitude of an individual element in $R_a^{h,l}$. We also calculate $\bar{\delta} = \frac{1}{N_h N_l} \sum_{h=1}^{N_h} \sum_{l=1}^{N_l} \text{AABS}(\text{SUB}(R_r^{h,l}, R_a^{h,l}))$ to evaluate the average magnitude of the differences between the elements of $R_r^{h,l}$ and $R_a^{h,l}$.

$\bar{\delta}/\bar{\epsilon}$	IMDb	arXiv	Cocktail	HumanEval	PG-19
Mistral-v0.3 7B	$8.3e-5$	$1.8e-4$	$7.1e-5$	$4.5e-5$	$5.6e-5$
	$6.43e-2$	$6.41e-2$	$6.44e-2$	$6.43e-2$	$6.39e-2$
Llama-3.1 8B	$1.1e-4$	$1.5e-4$	$8e-5$	$1.7e-4$	$1.4e-4$
	$5.29e-2$	$5.27e-2$	$5.28e-2$	$5.3e-2$	$5.25e-2$
Phi-3 14B	$1.9e-4$	$5.2e-5$	$1.1e-4$	$4.6e-5$	$1.3e-4$
	$5.41e-2$	$5.43e-2$	$5.44e-2$	$5.44e-2$	$5.41e-2$
Yi 34B	$1.7e-4$	$4.9e-5$	$7.6e-5$	$1.2e-4$	$8.9e-5$
	$5.05e-2$	$5.08e-2$	$5.06e-2$	$5.06e-2$	$5.11e-2$
Llama-3.1 70B	$9.5e-5$	$1.3e-4$	$8.4e-5$	$1.6e-4$	$1.02e-4$
	$5.54e-2$	$5.53e-2$	$5.54e-2$	$5.52e-2$	$5.51e-2$

Table 2. $\bar{\epsilon}$ and $\bar{\delta}$ for the Q_p - K_p pair.

Table 2 presents $\bar{\epsilon}$ and $\bar{\delta}$, displayed in the format $\bar{\delta}/\bar{\epsilon}$. We observe that the average variation $\bar{\delta}$ in the values of individual elements of R is less than 0.34% of the average absolute value $\bar{\epsilon}$ of a single element. This upper limit is derived from the results for Yi 34B with IMDb. This indicates that the R_p derived from random tokens is highly similar to the R derived from a different dataset, with minimal variation. Therefore,

the R is independent of tokens. In other words, the R_r computed offline from random tokens can be applied to other datasets to compress Q_p and K_p online. The explanation for this observation is detailed in §4.3.

To sum up, post-RoPE Q_p and K_p have a common rotation matrix R that can compress them without significantly distorting the data. The common R is independent of the tokens and only specific to the model. These two observations give us opportunities to accelerate attention and eliminate the K -decompression overhead in Palu.

4 Understanding Observations

In this section, we provide essential information and explanations to facilitate a deeper understanding of the observations presented in the motivation.

4.1 SVD for Data Compression in NLP

In NLP, SVD is widely used to reduce data dimensionality with low or even zero loss.

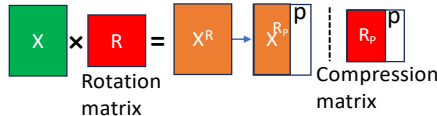


Figure 4. SVD for data compression.

Given a matrix X where each row represents an item’s vector to be compressed, X can be decomposed into $X = U\Sigma R^T$. U and R are rotation matrices, while Σ is a diagonal matrix filled with zeros except for non-negative singular values sorted in descending order along the diagonal. This decomposition, solvable using an SVD solver [44], has a unique solution. Singular values quantify the magnitude of vectors’ components after rotation by R . Consequently, each row of $X^R = XR$ is a rotated vector with elements decreasing from left to right, and the right p fraction of the columns of X^R can be discarded with minimal impact on vector relationships. This creates a compressed matrix X^{R_p} , with R_p as the compression matrix, as depicted in Fig. 4. To decompress the data, we only need to use the inverse of R , equivalent to R^T for rotation matrices, to rotate the compressed vectors back to their original orientation. Since the deleted dimensions can be considered zero-valued, we do not require the full R^T for decompression; instead, R_p^T suffices.

For any set of vectors we want to compress, such as all the row vectors of Q_p and K_p , we can arrange these vectors as rows to form the matrix X shown in Fig. 4. We then obtain the singular values and the matrix R used for compressing the vectors following the method described above. As long as the singular values contain many small values, it indicates that the set of vectors can be compressed using R without incurring significant loss.

4.2 Why Are Post-RoPE Q_p and K_p Compressible?

In §3.2, our experiments show that the post-RoPE Q_p and K_p exhibit many low-magnitude singular values after SVD decomposition, indicating that Q_p and K_p can be compressed using a matrix R without introducing significant loss. But

why do Q_p and K_p exhibit this property? Prior work [24, 32] has demonstrated that the pre-RoPE Q and K possess a low-rank property, meaning that their SVD decompositions yield many low-magnitude singular values. This suggests that Q and K have many dimensions in the space where their magnitudes are very small.

From a geometric perspective, the RoPE operation applied to Q and K rotates each vector within the plane formed by every pair of dimensions. Such rotational transformations do not amplify the vector magnitudes along the two dimensions that define each plane. Therefore, if a vector initially exhibits low magnitudes along the dimensions forming a plane, the RoPE rotation will preserve these low magnitudes post-transformation. Since Q and K naturally possess many dimensions with low magnitude, after RoPE, the corresponding dimensions with low magnitude that can form a plane in RoPE will also retain low magnitudes. This geometric behavior explains why Q_p and K_p still have low-magnitude dimensions and why the singular values of Q_p and K_p continue to exhibit many small values.

Because Q_p and K_p both have many low-magnitude dimensions, if they share many common low-magnitude dimensions, then performing SVD decomposition on all vectors of Q_p and K_p together will produce singular values with many small values. Fig. 3 has already shown that these singular values contain many small values, indicating that Q_p and K_p have common low-magnitude dimensions and therefore can be compressed using a common R .

4.3 Why Is the Common R for Q_p and K_p Independent of Tokens?

The singular values and the common R obtained by performing SVD decomposition on all vectors of Q_p and K_p are correlated. The singular values represent the magnitudes of all dimensions of the vectors after rotation by R . To answer why the common R is independent of tokens is to answer why the distribution of singular values is independent of tokens. Since the singular values reflect the dimension magnitudes of Q_p and K_p , this question can be further rephrased as why the low-magnitude dimensions of Q_p and K_p are independent of tokens.

Existing work has shown that the pre-RoPE Q and K have a low-rank property, and that the low-magnitude dimensions of Q and K are independent of tokens but related to model parameters [24, 32]. We take Q as an example to explain the reason. Since $Q = EW$, we can perform SVD decomposition on W to obtain $W = U\Sigma R^T$, resulting in $Q = EU\Sigma R^T$. Here, Σ and R are the singular values and the rotation matrix used for compression of Q . Σ originates from the parameter W and is unrelated to the token embedding E , so the distribution of dimension magnitudes in Q depends only on the model parameters and is independent of the tokens. The same holds for K . Importantly, since the RoPE operation is also independent of the token embedding E , the distribution of dimension

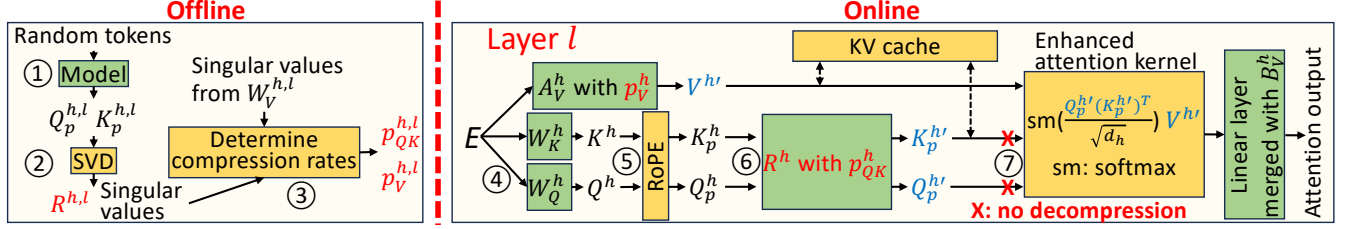


Figure 5. Overview.

magnitudes in the post-RoPE Q_p and K_p also depends only on the parameters and is independent of the tokens. Therefore, the singular values and R obtained by decomposing Q_p and K_p are independent of tokens. This also explains why the R obtained using different datasets (even random tokens) is highly similar.

5 Design

We detail our design in this section. Fig. 5 gives an overview of our approach, which consists of two stages: an offline stage and an online stage. The offline stage is responsible for obtaining the rotation matrix R used to compress Q_p and K_p , as well as the compression rate p for Q_p , K_p , and V under different accuracy constraints. The online stage performs inference using the R and p obtained during the offline stage under an accuracy constraint.

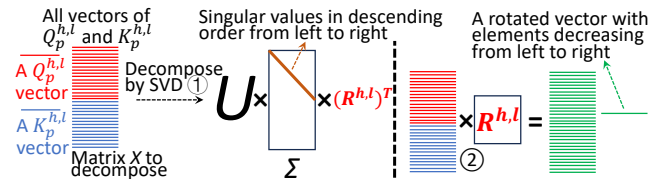
In the offline stage, we first randomly generate tokens and feed them into the model to extract $Q_p^{h,l}$ and $K_p^{h,l}$ from each head h in layer l (step ①). We then apply SVD to $Q_p^{h,l}$ and $K_p^{h,l}$ to obtain their singular values and the rotation matrix $R^{h,l}$ (step ②), as explained in §5.1. Since different heads contribute unequally to inference results [16, 18], we determine the compression rate p for Q_p , K_p , and V based on the singular values (step ③), with the goal of maximizing the overall KV compression rate under an accuracy constraint. Details are provided in §5.2. In the online stage, for each layer l , token embeddings E are linearly transformed by parameters W_Q^h and W_K^h to produce Q^h and K^h (step ④), which are then processed by RoPE to generate Q_p^h and K_p^h (step ⑤). These are subsequently compressed into $Q_p^{h'}$ and $K_p^{h'}$ using the rotation matrix R^h and compression rate p_{QK}^h shared by Q and K (step ⑥), following the method shown in Fig. 4. The compressed $Q_p^{h'}$ and $K_p^{h'}$ are directly used in the attention without requiring decompression. The compression method for V follows Palu but uses the compression rate p_V^h determined in step ③ to maximize overall KV compression rate. The compressed $V^{h'}$ is also fed directly into attention. Since Q_p^h , K_p^h , and V^h have different compression rates, the workload across SMs of the GPU during attention computation may become imbalanced. To address this, we design an enhanced attention kernel that balances SM workloads to accelerate attention computation (step ⑦). Details are provided in §5.3.

5.1 Post-RoPE QK Compression

Achieving K -decompression elimination and attention acceleration requires calculating the common R for post-RoPE Q_p and K_p as indicated in §3. We explain how to find the common R and use it to compress post-RoPE Q_p and K_p .

We begin by generating a series of random tokens and feeding them into the model to extract the post-RoPE representations $Q_p^{h,l}$ and $K_p^{h,l}$ from each head h in every layer l . As illustrated in Fig. 6, for each head h in layer l , we concatenate all vectors from $Q_p^{h,l}$ and $K_p^{h,l}$ row-wise to form a matrix X . The matrix X is then decomposed using SVD as $U\Sigma(R^{h,l})^T$ (step ① in Fig. 6). The singular values are located on the diagonal of Σ . The matrix $R^{h,l}$ serves as the rotation matrix used to rotate the vectors in $Q_p^{h,l}$ and $K_p^{h,l}$. After step ② in Fig. 6, the green rotated vectors obtained through $R^{h,l}$ are still arranged row-wise, and each rotated vector has elements arranged in descending order from left to right, a consequence of the singular values' arrangement in Σ . In other words, the magnitude of the singular values on the diagonal determines the relative size of each element in the rotated vectors. The larger the singular value, the greater the element value in the corresponding dimension, and vice versa. If we want to remove the smallest N elements from each rotated vector, we simply need to delete the rightmost N columns of $R^{h,l}$ before performing step ② in Fig. 6, as introduced in §4.1. Therefore, given a compression rate p_{QK}^h for Q_p^h and K_p^h , to compress $Q_p^{h,l}$ and $K_p^{h,l}$, we need to delete the rightmost $p_{QK}^h d_h$ columns of $R^{h,l}$ before performing step ②.

If the model uses Group Query Attention (GQA), we pair each query head's Q_p with its key head's K_p to compute the singular values and the rotation matrix R .

Figure 6. An example of compressing $Q_p^{h,l}$ and $K_p^{h,l}$.

How many random tokens do we need? The experimental results shown in Fig. 14 help us answer this question. For a given model, we observe that at least 8K random tokens are required to ensure the accuracy of the computed rotation matrix R . This is because a larger number of random tokens

allows for a more accurate identification of the common low-magnitude dimensions in $Q_p^{h,l}$ and $K_p^{h,l}$.

Does the introduced compression overhead (step ⑥ in Fig. 5) compromise the benefits from decompression elimination and attention acceleration? The answer to this question is negative. Experimental results in §6.8 show that the compression overhead is negligible compared to the overall JCT. We analyze why the introduced online compression overhead is small by examining both the prefill and decode phases. In the prefill phase, the computational complexity of attention is $8sd^2 + 4s^2d$, while all other linear layers have a complexity of $4sdd_{ff}$ [16], where d_{ff} is the size of the feed-forward neural network and larger than d . The compression of Q_p and K_p has a complexity of only $4sdd_h$. Since $d_h = 128$ is typically 32 to 64 times smaller than d , $4sdd_h$ is significantly smaller than $(8sd^2 + 4s^2d) + (4sdd_{ff}) = 8sd^2 + 4s^2d + 4sdd_{ff}$. It can be even smaller when the sequence length s is extremely long. This explains why the compression overhead during prefill is negligible. In the decode phase, the computational complexity of attention is $8d^2 + 4sd$, while all other linear layers have a complexity of $4dd_{ff}$ [16]. The compression of Q_p and K_p has a complexity of only $4dd_h$. $4dd_h$ is also significantly smaller than $(8d^2 + 4sd) + (4dd_{ff}) = 8d^2 + 4sd + 4dd_{ff}$, especially when the total sequence length s is extremely long. This explains why the compression overhead during decode is also negligible.

5.2 Adaptive Compression Rate Determination

Model layers contribute differently to the output [16], as do the attention heads within each layer [18]. This implies that different heads h in each layer l can have different compression rates. How to determine the compression rates for post-RoPE $Q_p^{h,l}$ and $K_p^{h,l}$, as well as $V^{h,l}$ when performing hidden dimension compression remains a question. Since different heads contribute differently, we expect that the distribution of singular values obtained through SVD for post-RoPE $Q_p^{h,l}$ - $K_p^{h,l}$ and $V^{h,l}$ may vary across different heads and layers. The singular values of $V^{h,l}$ are obtained by decomposing the model parameter $W_V^{h,l}$ through SVD [32]. Table 3 and Table 4 presents the coefficient of variation (CV) of the maximum singular values (i.e., those in the first head dimension) for $Q_p^{h,l}$ - $K_p^{h,l}$ and $V^{h,l}$ across all heads of each model with different datasets. The CV is the ratio of the standard deviation to the mean of the maximum singular values of heads. This CV for different models and datasets is around 40%-50%, indicating variation in the maximum singular values among different heads.

Since the dominant maximum singular values vary across heads, the compression rate p for each head should also differ. For heads with larger maximum singular values and more dimensions with relatively smaller values, we can use a higher p to remove more low-magnitude dimensions. Conversely, for heads with smaller maximum singular values and

	IMDb	arXiv	Cocktail	HumanEval	PG-19
Mistral-v0.3 7B	49.76%	49.55%	49.93%	50.04%	54.5%
Llama-3.1 8B	51.13%	51.21%	51.07%	50.94%	52.1%
Phi-3 14B	52.97%	53.38%	52.63%	52.53%	50.7%
Yi 34B	55.21%	55.73%	54.95%	54.98%	54.9%
Llama-3.1 70B	57.75%	58.03%	57.69%	57.51%	59.2%

Table 3. CV of the maximum singular values for $Q_p^{h,l}$ - $K_p^{h,l}$.

	IMDb	arXiv	Cocktail	HumanEval	PG-19
Mistral-v0.3 7B	41.86%	42.37%	41.44%	41.31%	43.55%
Llama-3.1 8B	43.59%	43.63%	43.56%	43.61%	42.92%
Phi-3 14B	45.37%	44.82%	44.96%	45.69%	44.73%
Yi 34B	44.48%	44.81%	44.96%	44.52%	45.25%
Llama-3.1 70B	45.16%	45.42%	45.38%	44.95%	45.58%

Table 4. CV of the maximum singular values for $V^{h,l}$.

fewer dimensions with relatively smaller values, we can use a lower p to remove fewer low-magnitude dimensions. This can achieve a higher overall compression rate p with minimal accuracy loss. How to determine p for $Q_p^{h,l}$ - $K_p^{h,l}$ and $V^{h,l}$ in each head? Since singular values represent the magnitude of the components of rotated vectors in their corresponding dimensions, the proportion of the cumulative sum of the removed singular values to the total sum of singular values determines the extent of information loss. We introduce a singular value removal rate r to control this proportion, which is the ratio of the sum of the singular values in the removed dimensions to the total sum of the singular values across all d_h dimensions. In a head, given an r , the corresponding p for $Q_p^{h,l}$ - $K_p^{h,l}$ and $V^{h,l}$ can be determined. Specifically, given an r , we only need to find p that satisfies the following condition:

$$\frac{\sum_{i=j+1}^{d_h-1} \theta^i}{\sum_{i=0}^{d_h-1} \theta^i} \leq r < \frac{\sum_{i=j}^{d_h-1} \theta^i}{\sum_{i=0}^{d_h-1} \theta^i} \text{ AND } j = \lfloor (1-p)(d_h-1) \rfloor, \quad (1)$$

where θ^i is the singular value at head dimension i . We set a shared r for all heads across different layers, allowing us to directly determine the p required for $Q_p^{h,l}$ - $K_p^{h,l}$ and $V^{h,l}$ in each head, thus obtaining an overall KV compression rate, which corresponds to an accuracy constraint. This enables us to construct a function F_p that takes an accuracy constraint as input and outputs a combination of p needed for all heads under this constraint. During inference, given an accuracy constraint, we use F_p to directly obtain the p needed for $Q_p^{h,l}$ - $K_p^{h,l}$ and $V^{h,l}$ in each head.

5.3 Kernel Enhancement for Adaptive Compression Rate

State-of-the-art memory-efficient attention kernel implementations (e.g., FlashAttention-2 [45]) operate as shown in Fig. 7. The attention computation of a batch of requests is divided into $batch_size \times N_h$ computation units, each corresponding to a head of a request. Each unit further splits Q into blocks of

shape ($B_r = 64, d_{qk} = d_h$), where B_r is the row block size and d_{qk} is the head dimension size for Q and K . Each Q block is processed on one SM as an SM task. All SMs responsible for a head share that head's K and V to minimize data movement between SMs, thereby reducing memory access overhead. When an SM processes a Q block, K , and V , it further divides K and V into blocks of shape ($B_c = 64, d_v = d_h$) to be processed sequentially in time order, where B_c is the column block size and d_v is the head dimension size for V . Without adaptive compression rates, all heads use the same d_{qk} and the same d_v . However, with adaptive compression rates, different heads have different d_{qk} and different d_v , resulting in varying computational loads and uneven execution times for each SM. The kernel runtime is determined by the SM with the longest execution time. Therefore, it is necessary to enhance the attention kernel with adaptive compression rates. We propose different enhancements for prefill and decode.

Prefill. During prefill, the computational workload of an SM task includes $2B_r d_{qk} s_{kv}$ for multiplying the Q block with K , $2B_r s_{kv}$ for soft-max, and $2B_r s_{kv} d_v$ for

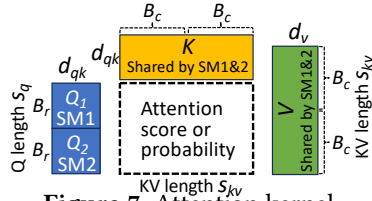


Figure 7. Attention kernel.

multiplying attention probability with V , resulting in a total of $2B_r s_{kv} (d_{qk} + d_v + 1)$, where s_{kv} is the sequence length of K and V . Let $d_{sum}^i = d_{qk} + d_v + 1$ for head i and d_{sum}^{max} be the maximum d_{sum}^i across all heads. As the compression rate changes, d_{sum}^i changes accordingly. We increase B_r to $\frac{d_{sum}^{max}}{d_{sum}^i} B_r$ for head i , ensuring that the computational workload for each SM task is the same, preventing uneven execution times among SMs. By increasing B_r , the number of Q blocks per head decreases, reducing the total number of SM tasks. As a result, the GPU can complete all SM tasks in fewer rounds, with each round using all SMs of the GPU. In the final round, not all SMs may be fully utilized. To maximize the utilization, we redistribute the remaining SM tasks in the last round. Suppose the GPU has N_{SM} SMs and the last round has N_{last} SM tasks. The workload assigned to each SM should be $wl = \frac{1}{N_{SM}} \sum_{i=1}^{N_{last}} B_r^{tsk(i)} d_{sum}^{tsk(i)}$, where $B_r^{tsk(i)}$ and $d_{sum}^{tsk(i)}$ is B_r and d_{sum} of the i -th SM task in the last round. Then, task i should be split into smaller blocks using new row block size $wl/d_{sum}^{tsk(i)}$. All redistributed tasks in the last round are sequentially assigned to an SM with the smallest allocated workloads one at a time.

Decode. In decode, the Q length s_q for each head is only 1, meaning it cannot be divided into multiple Q blocks. Consequently, each

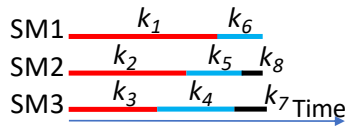


Figure 8. Task allocation.

head corresponds to one SM task, and adjusting B_r to enhance the kernel is not feasible. Instead, we schedule these

tasks in a heuristic way to avoid heavy overhead. The execution time of each task k_i is determined by $s_{kv} \times d_{sum}$. All tasks are sorted in descending order of execution time and then sequentially assigned to an SM with the smallest cumulative assigned time one at a time. Fig. 8 provides an example where 7 tasks are distributed across 3 SMs. Tasks k_1 - k_7 are sorted in descending order of execution time. Following our scheduling strategy, k_1 and k_6 are assigned to SM1, k_2 , k_5 , and k_8 to SM2, and k_3 , k_4 , and k_7 to SM3.

6 Performance Evaluation

6.1 Implementation

We implemented FDC based on vLLM [46] and modified vLLM model classes to enable QKV compression and adaptive compression rates. We used NVIDIA CUTLASS [47] to implement the on-device matrix multiplication for the attention kernel. A load balancer was implemented with a fast Python web framework Quart [48], which allocates each request to a vLLM instance with the shortest queue length.

Kernel enhancement for prefill. For prefill-phase kernel enhancement (§5.3), a large B_r can cause data to exceed the register capacity of a single SM. In such cases, we reduce B_c to prevent this issue, which does not affect the total computational workload of an SM task since s_{kv} remains unchanged. Limited by the tensor core interface used for matrix operations, the values of d_{qk} , d_v , B_r , and B_c must be multiples of 16. Therefore, these values are rounded up to the nearest multiple of 16, and any padding required is filled with zeros. For a given overall KV compression rate p , the d_{sum} and B_c for each head are determined, and B_r used by each head is also determined except in the final round. In the last round, B_r can be enumerated among multiples of 16. For different overall KV compression rates, we pre-compile all kernels offline according to the required matrix shapes.

Kernel enhancement for decode. For decode-phase kernel enhancement, we fused the scheduling computations (a significant portion of which involves sorting) to a CUDA kernel, thereby minimizing the time overhead.

6.2 Setup

In the evaluation, unless otherwise specified, we utilized the following settings. Table 5 lists the state-of-the-art models we used with their Tensor Parallelism (TP) and Pipeline Parallelism (PP) size, following the setting in [49, 50]. We used the datasets listed in Table 6. IMDb includes 27 genres of movies, TV shows, etc., collected on the Internet. It is operated by IMDb.com, Inc., a subsidiary of Amazon. The arXiv summarization has a collection of scientific publications and their summaries on arXiv.org [51]. Information Retrieval (IR) is the process of retrieving relevant content from vast amounts of information based on a user query. The Cocktail is a benchmark for IR, including 8 different IR tasks such as question answering, fact checking, etc. HumanEval evaluates the performance of code completion, including 164

programming problems. The Google PG-19 dataset provides a description of a book passage and requires the model to generate a book of a specified length. For the summarization and book generation tasks, we use *ROUGE-1* [52] as the accuracy metric; for the code completion task, we use *Edit Similarity (normalized Levenshtein distance)* [53, 54].

Mistral-v0.3 7B [37]	no TP and PP	Llama-3.1 8B [38]	no TP and PP
Phi-3 14B [39]	no TP and PP	Yi 34B [40]	TP=4
Llama-3.1 70B [38]	TP=4		

Table 5. Model size and TP/PP size.

Trace	Input length			Output length		
	avg	min	max	avg	min	max
IMDb classification [55]	315	106	821	37	16	87
arXiv summarization [34]	6.3K	1.6K	14.1K	243	29	464
Cocktail for IR [35]	49.7K	9.4K	104.9K	159	44	246
HumanEval [56]	204	75	697	139	11	552
Google PG-19 [36]	277	138	419	61.5K	24.3K	97.5K

Table 6. Trace properties.

We employed four AWS p4de.24xlarge instances [57] located in four nodes. Each instance is equipped with 8 NVIDIA A100 GPUs (each with 80 GiB memory), 96 vCPUs, and 1152 GiB host memory, connected with a 400 Gbps network. As in [58], we executed 16 concurrent clients to dispatch requests from a single dataset. We built our system atop vLLM [46] and scheduled each request to a vLLM instance (which holds one model replica) that has the shortest queue length [59], defined by the number of tokens. By default, the request rate is set to the maximum processing capacity without increasing queuing time, based on a Poisson distribution. The batch size is automatically determined by vLLM based on the available space in the KV cache.

6.3 Compared Methods

We selected Palu as our comparison method. FDC and Palu compress the hidden dimension of KV data, which complements token eviction-based and quantization-based methods. Thus, both FDC and Palu can be combined with them to improve compression rates further [32]. We selected the most representative state-of-the-art eviction-based method, Keyformer [22], and quantization-based method, KVQuant [31]. We combined FDC with Keyformer and KVQuant to create enhanced versions, referred to as KF-F and KVQ-F, respectively. We also combined Palu with Keyformer and KVQuant, denoted by KF-P and KVQ-P, respectively.

KF-F and KF-P. KF-F and KF-P apply Keyformer to evict KV and then use FDC and Palu to obtain compressed KV, respectively. Subsequent steps remain the same as FDC and Palu.

KVQ-F and KVQ-P. KVQ-F and KVQ-P first use FDC and Palu to obtain compressed KV, respectively, and then apply KVQuant to quantize the compressed KV. Before FDC’s attention and Palu decompressing K , the quantized KV is

dequantized. Subsequent steps remain the same as FDC and Palu.

	FDC	Palu	KF-F	KF-P	KVQ-F	KVQ-P
Mistral-v0.3 7B	0.61	0.55	0.71	0.68	0.90	0.88
Llama-3.1 8B	0.53	0.51	0.72	0.69	0.89	0.88
Phi-3 14B	0.58	0.50	0.80	0.75	0.92	0.90
Yi 34B	0.55	0.49	0.75	0.71	0.92	0.91
Llama-3.1 70B	0.63	0.57	0.74	0.72	0.91	0.89

Table 7. Overall KV compression rate (IMDb).

	FDC	Palu	KF-F	KF-P	KVQ-F	KVQ-P
Mistral-v0.3 7B	0.64	0.59	0.84	0.81	0.92	0.90
Llama-3.1 8B	0.65	0.55	0.84	0.82	0.90	0.88
Phi-3 14B	0.62	0.55	0.82	0.80	0.91	0.89
Yi 34B	0.64	0.57	0.87	0.84	0.91	0.90
Llama-3.1 70B	0.67	0.58	0.86	0.82	0.92	0.90

Table 8. Overall KV compression rate (arXiv).

	FDC	Palu	KF-F	KF-P	KVQ-F	KVQ-P
Mistral-v0.3 7B	0.58	0.51	0.79	0.75	0.90	0.89
Llama-3.1 8B	0.56	0.50	0.75	0.70	0.91	0.89
Phi-3 14B	0.67	0.59	0.82	0.77	0.92	0.90
Yi 34B	0.60	0.55	0.83	0.78	0.92	0.91
Llama-3.1 70B	0.59	0.52	0.84	0.76	0.92	0.89

Table 9. Overall KV compression rate (Cocktail).

	FDC	Palu	KF-F	KF-P	KVQ-F	KVQ-P
Mistral-v0.3 7B	0.53	0.50	0.73	0.69	0.89	0.89
Llama-3.1 8B	0.54	0.48	0.76	0.72	0.87	0.89
Phi-3 14B	0.54	0.50	0.77	0.72	0.91	0.90
Yi 34B	0.59	0.53	0.78	0.73	0.90	0.91
Llama-3.1 70B	0.56	0.52	0.77	0.74	0.87	0.89

Table 10. Overall KV compression rate (HumanEval).

6.4 Comparison of Compression Rates

We study the overall KV compression rate p given an accuracy constraint for different methods. Specifically, we focus on the scenarios where the methods achieve 99% of the baseline accuracy that is achieved without compression [22]. For KF-F, we configure the FDC and Keyformer components to contribute equally to the overall compression rate. KF-P follows the same way. Since KVQuant can only be configured with 2-4 quantization bit widths, we use 4-bit quantization for KVQuant, KVQ-F, and KVQ-P to ensure the accuracy can reach 99% of the baseline accuracy without compression. We use binary search to determine the maximum p that achieves 99% of the baseline accuracy. Table 7-11 show the results for different datasets. FDC alone achieves p of 0.53-0.67 across all datasets, while Palu achieves around 0.06 smaller p than FDC. KF-F and KVQ-F have around 0.04 and 0.01 higher p

	FDC	Palu	KF-F	KF-P	KVQ-F	KVQ-P
Mistral-v0.3 7B	0.65	0.58	0.81	0.77	0.92	0.91
Llama-3.1 8B	0.63	0.56	0.83	0.80	0.91	0.89
Phi-3 14B	0.66	0.59	0.79	0.74	0.91	0.90
Yi 34B	0.65	0.57	0.78	0.80	0.92	0.91
Llama-3.1 70B	0.67	0.59	0.83	0.79	0.91	0.89

Table 11. Overall KV compression rate (PG-19).

than KF-P and KVQ-P, respectively. The improvement stems from the adaptive compression rate introduced in FDC. KF-F, KVQ-F, KV-P, and KVQ-P all have higher compression rates than FDC and Palu, indicating the enhanced version of Keyformer and KVQuant can improve the compression rates further.

6.5 Overall System Performance

We tested Mistral-v0.3 7B, Phi-3 14B, Yi 34B, and Llama-3.1 70B, denoted by M, P, Y, and L. Since IMDb and HumanEval are both datasets with short sequences, we kept the popular dataset, HumanEval, and excluded IMDb. The KV compression rates for them follow those in Table 8-11 under the same accuracy constraint.

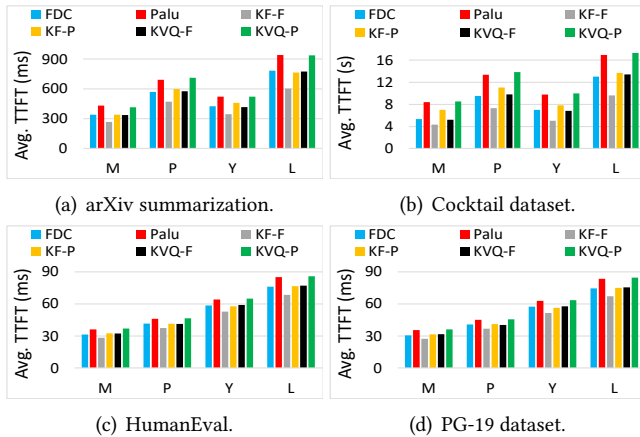


Figure 9. Average TTFT under different datasets.

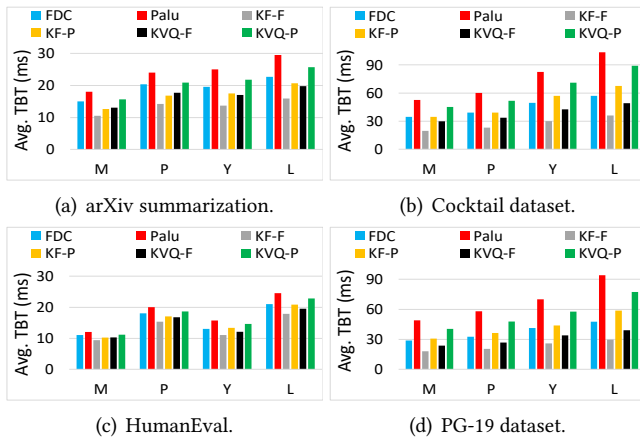


Figure 10. Average TBT under different datasets.

TTFT. Fig. 9 shows the average TTFT over requests for different models and datasets. For arXiv, Cocktail, HumanEval,

and PG-19, FDC reduces TTFT by 17%-21%, 20%-35%, 8%-13%, and 9%-12%, respectively, compared to Palu. This is because FDC not only reduces the K -decompression overhead but also computes on compressed data during attention, accelerating the attention computation. Additionally, FDC leverages adaptive compression rates and attention kernel enhancement to further reduce the attention time. The improvement is particularly significant for arXiv and Cocktail, as these datasets have longer input lengths, meaning that attention time constitutes a higher proportion of TTFT. Consequently, the reduction in attention time contributes more to the overall TTFT reduction. We observe a similar trend between KF-F and KF-P and between KVQ-F and KVQ-P, respectively. These improvements arise from the benefits provided by FDC, as described before. For a larger model, the improvement of FDC tends to be smaller because the proportion of attention time in TTFT tends to decrease.

TBT. Fig. 10 shows the average TBT over requests for different models and datasets. For arXiv, Cocktail, HumanEval, and PG-19, FDC reduces TBT by 16%-24%, 29%-54%, 11%-17%, and 46%-64%, respectively, compared to Palu. In addition to decompression overhead and attention acceleration, the improvement in TBT also stems from the reduced memory overhead due to the smaller KV size. There is a similar trend between KF-F and KF-P and between KVQ-F and KVQ-P, respectively. For a larger model, the improvement of FDC regarding TBT tends to increase because the proportion of K -decompression overhead in decode time tends to increase, which is eliminated by FDC. As shown in Fig. 1(b) and Fig. 2(b), the JCT for sequences with long output lengths is predominantly determined by the decode time. Therefore, for the long-output dataset PG-19, FDC achieves up to a 64% reduction in JCT compared to Palu.

Throughput study. We vary the overall throughput, Request Per Second (RPS), and record the normalized latency for each output token [46], calculated by dividing the end-to-end time (i.e., JCT) by the number of output tokens. Fig. 11 shows the normalized latency versus RPS for all models and datasets. When the RPS exceeds capacity, the queue length grows faster than the processing speed, leading to an infinite increase in queuing time and latency. Compared to Palu, FDC achieves 1.18-1.35 \times , 1.42-1.67 \times , 1.09-1.21 \times , and 1.53-1.97 \times RPS for arXiv, Cocktail, HumanEval, and PG-19, respectively, while preserving the same latency. The improvement is high for long-sequence datasets Cocktail and PG-19, because FDC eliminates the amplified decompression overhead and reduces the attention time. Additionally, the higher the KV compression rate, the higher the maximum RPS that can maintain a constant low latency. FDC benefits from the adaptive compression rates to have a higher overall compression rate and throughput. We observe a similar trend between KF-F and KF-P and between KVQ-F and KVQ-P, respectively, due to the same reason.

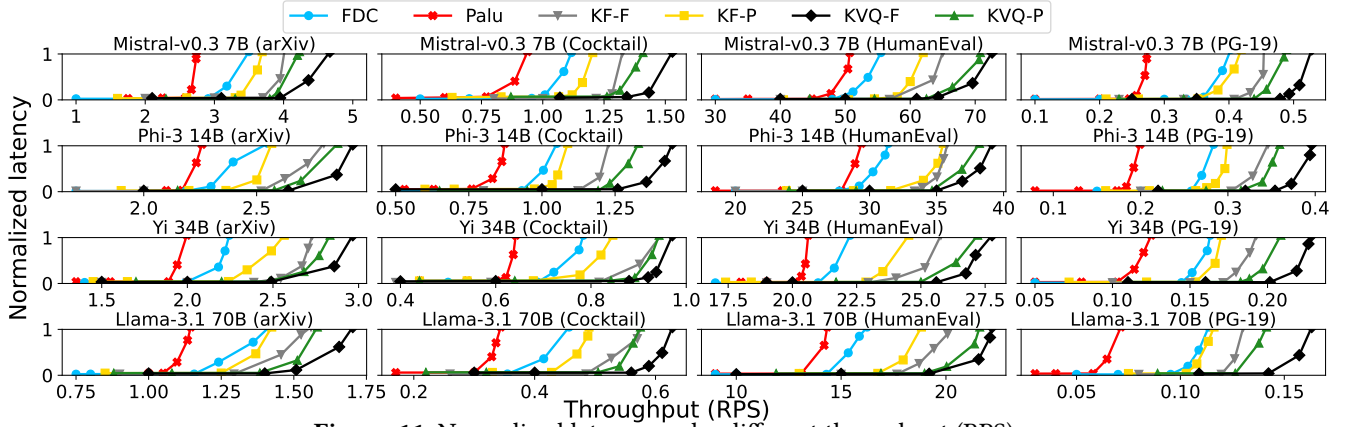


Figure 11. Normalized latency under different throughput (RPS).

6.6 Ablation Study

We test the variants of FDC as follows to evaluate each individual method. 1) FDC/PRC is FDC without Post-RoPE QK Compression for decompression overhead elimination and attention acceleration. It compresses K before RoPE and uses uncompressed K in attention, following Palu. 2) FDC/AC is FDC without Adaptive Compression rate. It uses the same compression rate for all heads to achieve 99% of the accuracy without compression. 3) FDC/KE is FDC without the attention Kernel Enhancement.

Fig. 12 and Fig. 13 show the average TTFT and TBT over requests for individual methods with different models and datasets. As shown in Fig. 12, /PRC has 5%-9%, 6%-17%, 4%-5%, and 4%-6% higher TTFT than FDC for arXiv, Cocktail, HumanEval, and PG-19 because /PRC performs K -decompression online and uses uncompressed data for attention computation. /AC has 3%-8%, 4%-10%, 3%-5%, and 3%-5% higher TTFT than FDC because, without the adaptive compression rate, the overall KV compression rate required to achieve 99% of the accuracy without compression is lower, thereby increasing attention time. /KE has 3%-9%, 4%-11%, 3%-6%, and 4%-5% higher TTFT than FDC due to the uneven computation times of SMs. In Fig. 13, /PRC has 11%-18%, 29%-34%, 4%-9%, and 31%-46% higher TBT than FDC for arXiv, Cocktail, HumanEval, and PG-19. /AC has 6%-9%, 8%-18%, 5%-7%, and 11%-19% higher TBT than FDC. /KE has 7%-13%, 10%-21%, 7%-8%, and 13%-22% higher TBT than FDC. The reasons for the TBT degradation of /AC and /KE are the same as explained for TTFT. /PRC has a higher TBT degradation compared to /AC and /KE because it has K -decompression overhead.

6.7 Sensitivity Testing

We vary the total number of random tokens used for the offline computation of R to study its impact on R . Given a specific number of randomly generated tokens, for each model’s Q_p - K_p pair, we calculate the ratio $\bar{\delta}/\bar{\epsilon}$ in §3.2 for each dataset and calculate their average across datasets. The smaller $\bar{\delta}/\bar{\epsilon}$, the more accurate R is. Fig. 14 shows this average

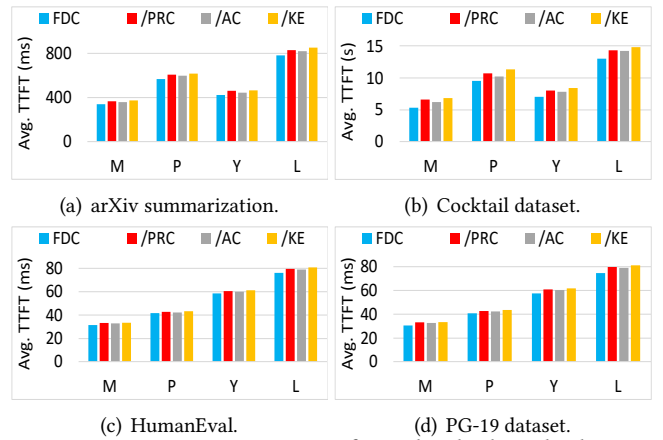


Figure 12. Average TTFT for individual methods.

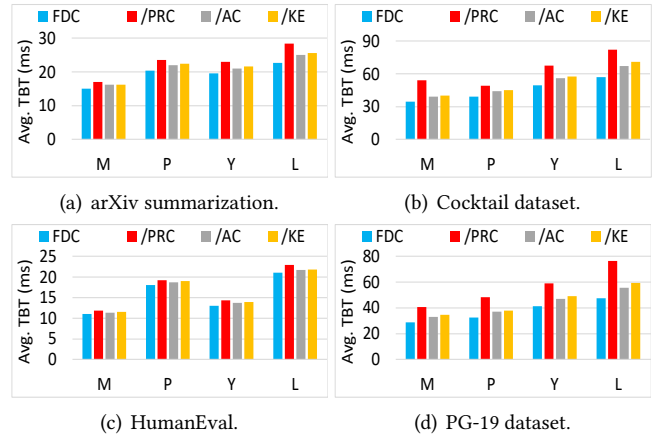


Figure 13. Average TBT for individual methods.

ratio across datasets for the Q_p - K_p pair of each model. The results show that when the number of random tokens is greater than 8K, the average ratio $\bar{\delta}/\bar{\epsilon}$ across datasets for all models is below 0.5%, ensuring the accuracy of the offline-computed R . The rationale for this has already been explained in §4.3 to support the conclusion in that section.

6.8 Time Overhead

We study the compression time overhead for multiplying R online and the time overhead introduced by SM scheduling

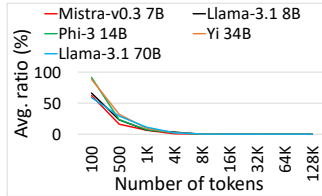


Figure 14. The average ratio $\bar{\delta}/\bar{\epsilon}$ across datasets.

in the attention kernel. We record the number of GPU cycles occupied by the scheduling computation and use this to estimate scheduling time. Finally, we calculate the proportion of time overhead relative to JCT. Table 12 presents the 99th percentile (P99) compression time overhead ratio for different models and datasets. The P99 compression time overhead is no more than 0.7% of JCT for all models and datasets, indicating that the compression time overhead is negligible compared to JCT. The reason has been explained in §5.1. Table 13 presents the P99 scheduling time overhead ratio for different models and datasets. As the model size increases and the input length becomes longer, the P99 time overhead ratio tends to decrease. This is because larger models and longer sequences spend more time on computation, thereby reducing the proportion of the overhead. The P99 time overhead does not exceed 4.13% of the end-to-end latency, making the scheduling overhead acceptable.

	arXiv	Cocktail	HumanEval	PG-19
Llama-3.1 8B	0.07%	0.09%	0.3%	0.05%
Phi-3 14B	0.08%	0.04%	0.5%	0.02%
Yi 34B	0.07%	0.01%	0.7%	0.09%
Llama-3.1 70B	0.05%	0.08%	0.4%	0.04%

Table 12. P99 compression overhead compared to JCT.

	arXiv	Cocktail	HumanEval	PG-19
Llama-3.1 8B	2.74%	2.37%	3.81%	1.27%
Phi-3 14B	2.37%	2.27%	3.54%	0.94%
Yi 34B	1.85%	1.64%	3.52%	0.85%
Llama-3.1 70B	2.39%	1.98%	3.75%	0.99%

Table 13. P99 kernel scheduling overhead compared to JCT.

7 Limitations and Discussion

Kernel enhancement. The enhancement of the attention kernel with adaptive compression rates relies on a simple heuristic method for workload scheduling. In the future, we will optimize this approach to minimize attention latency.

Storage of R . The rotation matrices R computed offline need to be stored in GPU memory, which incurs additional memory overhead. Fortunately, each attention head only requires a single R , and its shape is merely $d_h \times d_h$. The total number of parameters for all the matrices R typically accounts for less than 1% of the total parameter count of the model. Therefore, although storing R introduces some memory overhead, it is negligible compared to the overall model size.

8 Related Work

Low-rank approximation. Recently, Palu [32] has been proposed to use low-rank approximations to reduce the hidden size of KV. However, it still requires decompressing KV during attention and cannot compute on the compressed Q and K to reduce computation time for RoPE-based models. FDC not only eliminates decompression overhead but also reduces attention computation time by performing computation on the compressed Q and K .

Eviction. Many KV compression methods are based on token eviction [17–26], also known as pruning. The main idea is to remove unimportant tokens’ KV that have minimal impact on inference results. The methods in [17–24] determine token importance based on attention scores. Tokens with lower scores are considered less important, and their KV can be discarded. InfiniGen [24] leverages low-rank approximation for QK to identify low-score tokens efficiently. The methods in [25, 26] achieve sparse attention by identifying low-score regions in the attention score matrix and removing KV in those regions. Eviction-based methods reduce KV along the sequence dimension, while FDC reduces KV along the hidden dimension.

Quantization. Many methods use quantization to compress KV [27–31]. The basic idea is to compress each element of KV by reducing high-bit representations, such as float16, to lower-bit representations, such as 4-bit or even 2-bit. It reduces the number of bits required to store KV. However, during attention computation, the quantized KV must first be dequantized to recover the original data, introducing decompression overhead. FDC, on the other hand, reduces the total number of elements of K and V . As such, it can complement quantization methods. FDC can first compress the dimensionality of KV to reduce the total number of elements, followed by quantization to compress the individual elements.

9 Conclusion

In this paper, we introduce FDC, a fast KV dimensionality compression system that eliminates the K -decompression overhead in Palu and accelerates attention. It can serve as a complementary approach to existing eviction and quantization methods. FDC also adopts adaptive compression rates to maximize the overall KV compression rate under an accuracy constraint and leverages an enhanced attention kernel that balances SM workloads to improve attention latency. Comprehensive experiments show that FDC reduces JCT by up to 64% compared to Palu. When the state-of-the-art eviction and quantization methods are combined with FDC, they also outperform those combined with Palu.

References

- [1] Alec Radford, Karthik Narasimhan, Tim Salimans, Ilya Sutskever, et al. Improving language understanding by generative pre-training. 2018.
- [2] Jacob Devlin, Ming-Wei Chang, Kenton Lee, and Kristina Toutanova. BERT: pre-training of deep bidirectional transformers for language

- understanding. *CoRR*, abs/1810.04805, 2018.
- [3] Alec Radford, Jeffrey Wu, Rewon Child, David Luan, Dario Amodei, Ilya Sutskever, et al. Language models are unsupervised multitask learners. *OpenAI blog*, 1(8):9, 2019.
 - [4] Tom Brown, Benjamin Mann, Nick Ryder, Melanie Subbiah, Jared D Kaplan, Prafulla Dhariwal, Arvind Neelakantan, Pranav Shyam, Girish Sastry, Amanda Askell, Sandhini Agarwal, Ariel Herbert-Voss, Gretchen Krueger, Tom Henighan, Rewon Child, Aditya Ramesh, Daniel Ziegler, Jeffrey Wu, Clemens Winter, Chris Hesse, Mark Chen, Eric Sigler, Mateusz Litwin, Scott Gray, Benjamin Chess, Jack Clark, Christopher Berner, Sam McCandlish, Alec Radford, Ilya Sutskever, and Dario Amodei. Language models are few-shot learners. In H. Larochelle, M. Ranzato, R. Hadsell, M.F. Balcan, and H. Lin, editors, *Advances in Neural Information Processing Systems*, volume 33, pages 1877–1901. Curran Associates, Inc., 2020.
 - [5] Timo Schick, Jane Dwivedi-Yu, Roberto Dessi, Roberta Raileanu, Maria Lomeli, Luke Zettlemoyer, Nicola Cancedda, and Thomas Scialom. Toolformer: Language models can teach themselves to use tools, 2023.
 - [6] Meta llama-2 models. <https://huggingface.co/models?sort=trending&search=meta+Llama-2>, 2024.
 - [7] Textsynth: Text completion. <https://textsynth.com/completion.html>.
 - [8] Openai: ChatGPT. <https://chat.openai.com/>, [Accessed in Aug. 2023].
 - [9] GitHub Copilot. <https://github.com/features/copilot/>, 2025.
 - [10] Speaking your language: The transformer in machine translation. <https://blog.huawei.com/2022/02/01/speaking-your-language-transformer-machine-translation/>.
 - [11] Elozino Egonmwan and Yllias Chali. Transformer-based model for single documents neural summarization. In *Proceedings of the 3rd Workshop on Neural Generation and Translation*, pages 70–79, Hong Kong, November 2019. Association for Computational Linguistics.
 - [12] Zi Gong, Cuiyun Gao, Yasheng Wang, Wenchao Gu, Yun Peng, and Zenglin Xu. Source code summarization with structural relative position guided transformer. In *2022 IEEE International Conference on Software Analysis, Evolution and Reengineering (SANER)*, pages 13–24, 2022.
 - [13] Haopeng Zhang, Xiao Liu, and Jiawei Zhang. HEGEL: Hypergraph transformer for long document summarization, 2022.
 - [14] Ashutosh Adhikari, Achyudh Ram, Raphael Tang, and Jimmy Lin. Docbert: BERT for document classification. *CoRR*, abs/1904.08398, 2019.
 - [15] Xiang Dai, Ilias Chalkidis, Sune Darkner, and Desmond Elliott. Revisiting transformer-based models for long document classification, 2022.
 - [16] Ashish Vaswani, Noam Shazeer, Niki Parmar, Jakob Uszkoreit, Llion Jones, Aidan N Gomez, Łukasz Kaiser, and Illia Polosukhin. Attention is all you need. In I. Guyon, U. Von Luxburg, S. Bengio, H. Wallach, R. Fergus, S. Vishwanathan, and R. Garnett, editors, *Advances in Neural Information Processing Systems*, volume 30. Curran Associates, Inc., 2017.
 - [17] Zhenyu Zhang, Ying Sheng, Tianyi Zhou, Tianlong Chen, Lianmin Zheng, Ruisi Cai, Zhao Song, Yuandong Tian, Christopher Ré, Clark Barrett, Zhangyang "Atlas" Wang, and Beidi Chen. H2o: Heavy-hitter oracle for efficient generative inference of large language models. In A. Oh, T. Neumann, A. Globerson, K. Saenko, M. Hardt, and S. Levine, editors, *Advances in Neural Information Processing Systems*, volume 36, pages 34661–34710. Curran Associates, Inc., 2023.
 - [18] Suyu Ge, Yunan Zhang, Liyuan Liu, Minjia Zhang, Jiawei Han, and Jianfeng Gao. Model tells you what to discard: Adaptive kv cache compression for llms. *arXiv preprint arXiv:2310.01801*, 2023.
 - [19] Zichang Liu, Aditya Desai, Fangshuo Liao, Weitao Wang, Victor Xie, Zhaozhuo Xu, Anastasios Kyrillidis, and Anshumali Shrivastava. Scissorhands: Exploiting the persistence of importance hypothesis for llm kv cache compression at test time. In A. Oh, T. Neumann, A. Globerson, K. Saenko, M. Hardt, and S. Levine, editors, *Advances in Neural Information Processing Systems*, volume 36, pages 52342–52364. Curran Associates, Inc., 2023.
 - [20] Dongjie Yang, XiaoDong Han, Yan Gao, Yao Hu, Shilin Zhang, and Hai Zhao. Pyramidinfer: Pyramid kv cache compression for high-throughput llm inference, 2024.
 - [21] Alessio Devoto, Yu Zhao, Simone Scardapane, and Pasquale Minervini. A simple and effective l_2 norm-based strategy for KV cache compression. In Yaser Al-Onaizan, Mohit Bansal, and Yun-Nung Chen, editors, *Proceedings of the 2024 Conference on Empirical Methods in Natural Language Processing*, pages 18476–18499, Miami, Florida, USA, November 2024. Association for Computational Linguistics.
 - [22] Muhammad Adnan, Akhil Arunkumar, Gaurav Jain, Prashant Nair, Ilya Solovychik, and Purushotham Kamath. Keyformer: Kv cache reduction through key tokens selection for efficient generative inference. In P. Gibbons, G. Pekhimenko, and C. De Sa, editors, *Proceedings of Machine Learning and Systems*, volume 6, pages 114–127, 2024.
 - [23] Sotiris Anagnostidis, Dario Pavlo, Luca Biggio, Lorenzo Noci, Aurelien Lucchi, and Thomas Hofmann. Dynamic context pruning for efficient and interpretable autoregressive transformers. In A. Oh, T. Naumann, A. Globerson, K. Saenko, M. Hardt, and S. Levine, editors, *Advances in Neural Information Processing Systems*, volume 36, pages 65202–65223. Curran Associates, Inc., 2023.
 - [24] Wonbeom Lee, Jungi Lee, Junghwan Seo, and Jaewoong Sim. InfiniGen: Efficient generative inference of large language models with dynamic KV cache management. In *18th USENIX Symposium on Operating Systems Design and Implementation (OSDI 24)*, pages 155–172, Santa Clara, CA, July 2024. USENIX Association.
 - [25] Chaoran Zhang, Lixin Zou, Dan Luo, Min Tang, Xiangyang Luo, Zihao Li, and Chenliang Li. Efficient sparse attention needs adaptive token release, 2024.
 - [26] Huiqiang Jiang, YUCHENG LI, Chengruidong Zhang, Qianhui Wu, Xufang Luo, Surin Ahn, Zhenhua Han, Amir H. Abdi, Dongsheng Li, Chin-Yew Lin, Yuqing Yang, and Lili Qiu. MInference 1.0: Accelerating pre-filling for long-context LLMs via dynamic sparse attention. In *The Thirty-eighth Annual Conference on Neural Information Processing Systems*, 2024.
 - [27] Yefei He, Luoming Zhang, Weijia Wu, Jing Liu, Hong Zhou, and Bohan Zhuang. Zipcache: Accurate and efficient kv cache quantization with salient token identification, 2024.
 - [28] Hao Kang, Qingru Zhang, Souvik Kundu, Geonhwa Jeong, Zaoxing Liu, Tushar Krishna, and Tuo Zhao. GEAR: An efficient KV cache compression recipe for near-lossless generative inference of LLM. *arXiv preprint arXiv:2403.05527*, 2024.
 - [29] Zirui Liu, Jiayi Yuan, Hongye Jin, Shaochen Zhong, Zhaozhuo Xu, Vladimir Braverman, Beidi Chen, and Xia Hu. KIVI: A tuning-free asymmetric 2bit quantization for KV cache. In Ruslan Salakhutdinov, Zico Kolter, Katherine Heller, Adrian Weller, Nuria Oliver, Jonathan Scarlett, and Felix Berkenkamp, editors, *Proceedings of the 41st International Conference on Machine Learning*, volume 235 of *Proceedings of Machine Learning Research*, pages 32332–32344. PMLR, 21–27 Jul 2024.
 - [30] Yuhan Liu, Hanchen Li, Yihua Cheng, Siddhant Ray, Yuyang Huang, Qizheng Zhang, Kuntai Du, Jiayi Yao, Shan Lu, Ganesh Ananthanarayanan, Michael Maire, Henry Hoffmann, Ari Holtzman, and Junchen Jiang. Cachegen: Kv cache compression and streaming for fast large language model serving. In *Proceedings of the ACM SIGCOMM 2024 Conference*, ACM SIGCOMM '24, page 38–56, New York, NY, USA, 2024. Association for Computing Machinery.
 - [31] Coleman Hooper, Sehoon Kim, Hiva Mohammadzadeh, Michael W. Mahoney, Yakun Sophia Shao, Kurt Keutzer, and Amir Gholami. Kvquant: Towards 10 million context length llm inference with kv cache quantization, 2024.
 - [32] Chi-Chih Chang, Wei-Cheng Lin, Chien-Yu Lin, Chong-Yan Chen, Yu-Fang Hu, Pei-Shuo Wang, Ning-Chi Huang, Luis Ceze, Mohamed S. Abdelfattah, and Kai-Chiang Wu. Palu: KV-cache compression with

- low-rank projection. In *The Thirteenth International Conference on Learning Representations*, 2025.
- [33] Jianlin Su, Murtadha Ahmed, Yu Lu, Shengfeng Pan, Wen Bo, and Yunfeng Liu. Roformer: Enhanced transformer with rotary position embedding. *Neurocomput.*, 568(C), March 2024.
- [34] Arman Cohan, Franck Dernoncourt, Doo Soon Kim, Trung Bui, Seokhwan Kim, Walter Chang, and Nazli Goharian. A discourse-aware attention model for abstractive summarization of long documents, 2018.
- [35] Sunhao Dai, Weihao Liu, Yuqi Zhou, Liang Pang, Rongju Ruan, Gang Wang, Zhenhua Dong, Jun Xu, and Ji-Rong Wen. Cocktail: A comprehensive information retrieval benchmark with llm-generated documents integration, 2024.
- [36] Google PG-19. <https://github.com/google-deepmind/pg19>.
- [37] Mistral-v0.3. <https://huggingface.co/mistralai/Mistral-7B-Instruct-v0.3>, 2024.
- [38] Meta Llama-3.1. <https://llama.meta.com/>, 2024.
- [39] Microsoft Phi-3. <https://huggingface.co/microsoft/Phi-3-medium-128k-instruct>, 2024.
- [40] 01-ai model Yi. <https://huggingface.co/01-ai/Yi-34B-200K>, 2024.
- [41] Gemma Team. Gemma 2: Improving open language models at a practical size, 2024.
- [42] FDC code. <https://anonymous.4open.science/r/FastDC>, 2025.
- [43] V. Klema and A. Laub. The singular value decomposition: Its computation and some applications. *IEEE Transactions on Automatic Control*, 25(2):164–176, 1980.
- [44] Singular value decomposition solver from scipy. <https://docs.scipy.org/doc/scipy/reference/generated/scipy.linalg.svd.html>, 2024.
- [45] Tri Dao. Flashattention-2: Faster attention with better parallelism and work partitioning, 2023.
- [46] Woosuk Kwon, Zhuohan Li, Siyuan Zhuang, Ying Sheng, Lianmin Zheng, Cody Hao Yu, Joseph Gonzalez, Hao Zhang, and Ion Stoica. Efficient memory management for large language model serving with pagedattention. In *Proceedings of the 29th Symposium on Operating Systems Principles, SOSP '23*, page 611–626, New York, NY, USA, 2023. Association for Computing Machinery.
- [47] NVIDIA CUTLASS. <https://github.com/NVIDIA/cutlass>.
- [48] Quart. <https://quart.palletsprojects.com/en/latest/>.
- [49] Amey Agrawal, Nitin Kedia, Ashish Panwar, Jayashree Mohan, Nipun Kwatra, Bhargav Gulavani, Alexey Tumanov, and Ramachandran Ramjee. Taming Throughput-Latency tradeoff in LLM inference with Sarathi-Serve. In *18th USENIX Symposium on Operating Systems Design and Implementation (OSDI 24)*, pages 117–134, Santa Clara, CA, July 2024. USENIX Association.
- [50] Yinmin Zhong, Shengyu Liu, Junda Chen, Jianbo Hu, Yibo Zhu, Xuanzhe Liu, Xin Jin, and Hao Zhang. DistServe: Disaggregating prefill and decoding for goodput-optimized large language model serving. In *18th USENIX Symposium on Operating Systems Design and Implementation (OSDI 24)*, pages 193–210, Santa Clara, CA, July 2024. USENIX Association.
- [51] arxiv. <https://arxiv.org>.
- [52] Chin-Yew Lin. Rouge: A package for automatic evaluation of summaries. In *Text summarization branches out*, pages 74–81, 2004.
- [53] Lei Zhang, Yunshui Li, Jiaming Li, Xiaobo Xia, Jiayi Yang, Run Luo, Minzheng Wang, Longze Chen, Junhao Liu, and Min Yang. Hierarchical context pruning: Optimizing real-world code completion with repository-level pretrained code llms, 2024.
- [54] Gang Wu. String similarity metrics – edit distance. <https://www.baeldung.com/cs/string-similarity-edit-distance>, 2024.
- [55] Genre classification dataset imdb. <https://www.kaggle.com/datasets/hijest/genre-classification-dataset-imdb>.
- [56] Mark Chen, Jerry Tworek, Heewoo Jun, Qiming Yuan, Henrique Ponde de Oliveira Pinto, Jared Kaplan, Harri Edwards, Yuri Burda, Nicholas Joseph, Greg Brockman, Alex Ray, Raul Puri, Gretchen Krueger, Michael Petrov, Heidy Khlaaf, Girish Sastry, Pamela Mishkin, Brooke Chan, Scott Gray, Nick Ryder, Mikhail Pavlov, Alethea Power, Lukasz Kaiser, Mohammad Bavarian, Clemens Winter, Philippe Tillet, Felipe Petroski Such, Dave Cummings, Matthias Plappert, Fotios Chantzis, Elizabeth Barnes, Ariel Herbert-Voss, William Hebgen Guss, Alex Nichol, Alex Paino, Nikolas Tezak, Jie Tang, Igor Babuschkin, Suchir Balaji, Shantanu Jain, William Saunders, Christopher Hesse, Andrew N. Carr, Jan Leike, Josh Achiam, Vedant Misra, Evan Morikawa, Alec Radford, Matthew Knight, Miles Brundage, Mira Murati, Katie Mayer, Peter Welinder, Bob McGrew, Dario Amodei, Sam McCandlish, Ilya Sutskever, and Wojciech Zaremba. Evaluating large language models trained on code, 2021.
- [57] Amazon EC2 P4 instances. <https://aws.amazon.com/ec2/instance-types/p4/>.
- [58] Connor Holmes, Masahiro Tanaka, Michael Wyatt, Ammar Ahmad Awan, Jeff Rasley, Samyam Rajbhandari, Reza Yazdani Aminabadi, Heyang Qin, Arash Bakhtiari, Lev Kurilenko, and Yuxiong He. DeepSpeed-fastgen: High-throughput text generation for llms via mii and deepspeed-inference. *arXiv preprint arXiv:2401.08671*, 2024.
- [59] Pratyush Patel, Esha Choukse, Chaojie Zhang, Aashaka Shah, Íñigo Goiri, Saeed Maleki, and Ricardo Bianchini. Splitwise: Efficient generative llm inference using phase splitting. In *2024 ACM/IEEE 51st Annual International Symposium on Computer Architecture (ISCA)*, pages 118–132, 2024.